

Decoherent phonon effects in fast atom-surface scattering

L. Frisco¹ and M.S. Gravielle¹

¹*Instituto de Astronomía y Física del Espacio (UBA-CONICET),
Ciudad Universitaria, (C1428EGA) Buenos Aires, Argentina.*

(Dated: March 16, 2023)

The study of the influence of phonon-mediated processes on grazing-incidence fast atom diffraction (GIFAD) patterns is relevant for the use of GIFAD as a surface analysis technique. In this work, we apply the Phonon-Surface Initial Value Representation (P-SIVR) approximation to investigate lattice vibration effects on GIFAD patterns for the He/LiF(001) system at room temperature. The main features introduced by thermal lattice vibrations in the angular distributions of the scattered helium atoms are analyzed by considering normal energies in the 0.1 -3 eV range. In all the cases, thermal fluctuations introduce a wide polar spread that transforms the interference maxima into elongated strips. We found that the polar width of these maxima does not depend on the normal energy, as it was experimentally observed. In addition, when the normal energy increases, not only the relative intensities of interference peaks are affected by the crystal vibrations, but also the visibility of the interference structures, which disappear completely for normal energies approximately equal to 3 eV. These findings qualitatively agree with recent experimental data, but the simulated polar widths underestimate the experimentally-derived limit, suggesting that there are other mechanisms, such as inelastic phonon processes, that contribute to the polar dispersion of the GIFAD patterns.

I. INTRODUCTION

Grazing-incidence fast atom diffraction (GIFAD) has been the subject of extensive experimental and theoretical research since its first experimental reports in 2007 [1, 2]. From the theoretical point of view, significant advances have been reached in the description of GIFAD over these 15 years [3]. Different theoretical methods, which range from classical and semiclassical (or semi-quantum) approaches to full quantum calculations, have been applied to describe and analyze GIFAD experiments for a wide variety of crystal targets, not only at room temperature but also at higher temperatures [4]. But in the vast majority of these works, diffraction patterns were assumed to be produced by elastic scattering from ideal frozen crystal surfaces, with the atoms at rest at their equilibrium positions, whereas the contribution of lattice vibrations, i.e., phonons, was considered to play a minor role, as suggested in early articles [5–7]. However, the influence of phonon-mediated processes on GIFAD patterns is still not fully understood, becoming a topic that has recently attracted renewed interest [8–14].

The most remarkable effect introduced by phonons in GIFAD patterns from insulator surfaces is a wide polar dispersion of the projectile distribution [10, 13], a feature that was early predicted by Manson *et al.* [15]. While atomic projectiles elastically scattered off an ideal static surface hit the detector plane forming a thin annulus, named the Laue circle, as a consequence of the energy conservation [1, 2], the inclusion of lattice vibrations within the theoretical models transforms the interference maxima into elongated streaks along the polar angle, as it is usually observed in GIFAD experiments [10–13]. Hence, the polar profile of GIFAD patterns was the focus of recent experimental and theoretical works, where the variation of the polar-profile width as a function of both, the normal incidence energy [13] and the

sample's temperature [11, 14], was investigated. On the other hand, a systematic theoretical study of thermal vibration effects on the azimuthal characteristics of the interference patterns as a function of the incidence conditions is still missing.

In this paper, we use the He/LiF(001) system at room temperature, which is a prototype of the GIFAD phenomenon, as a benchmark to study how the phonon effects associated with the thermal fluctuations of the LiF lattice vary as the incidence conditions change. The aim is to analyze the dependence of such thermal effects on the normal incidence energy $E_{\perp} = E \sin^2 \theta_i$, with E being the total incidence energy and θ_i the glancing incidence angle. Notice that in typical GIFAD experiments, the interference structures of the projectile distributions are mainly governed by E_{\perp} [16, 17]. Consequently, the relative intensities of the interference maxima as a function of E_{\perp} are commonly employed to determine the electronic or morphological characteristics of the crystal surface [18]. This fact makes it relevant to know the influence of the normal energy in the thermal vibration effects on the diffraction patterns.

Our study is based on the Phonon-Surface Initial Value Representation (P-SIVR) approximation [10], which is a semiclassical method that accounts for phonon transitions using a quantum harmonic crystal model. Within the P-SIVR approach, the scattering probability is expressed as a series in terms of the net number of phonons exchanged during the atom-surface collision. The first-order term, P0-SIVR, associated with the zero-phonon scattering process [10, 11], is here applied to investigate the E_{\perp} -dependence of the lattice vibration effects on the angular distributions of He atoms grazing scattered off a LiF(001) surface along the $\langle 110 \rangle$ channel. The incidence conditions are chosen in accord with a recent experimental study for He/LiF(001) GIFAD by Debiossac *et al.* [12], which will be used for comparison.

The article is organized as follows. The P0-SIVR approach is summarized in Sec. II, while results are presented and discussed in Sec. III, analyzing the decoherent limit and the phonon effects on the polar profile. In Sec. IV we outline our conclusions. Atomic units (a.u.) are used unless otherwise stated.

II. THEORETICAL MODEL

The P-SIVR approximation is based on the previous Surface Initial Value Representation (SIVR) approach for grazing scattering from a rigid surface [19], which has been successfully applied to different GIFAD problems [20–24]. The basic idea of the P-SIVR and SIVR methods is to use the Van Vleck representation of the time-evolution quantum operator, as given by Miller [25], within the frame of a time-dependent distorted wave formalism [26]. This strategy makes it possible to describe the quantum interference effects involved in GIFAD in terms of classical trajectories with different initial conditions, incorporating an approximated representation of the classically forbidden transitions that contribute to the dark side of the rainbow angle. But in contrast with the SIVR approach, where the surface is represented by means of an ideal static crystal model, the P-SIVR approximation makes use of the harmonic crystal description [27], which allows us to take into account phonon-mediated processes.

Within the P-SIVR approach, the differential scattering probabilities associated with transitions between different initial and final crystal states are averaged over the equilibrium distribution of the initial phonon states, after adding over all the possible final states. Thus, the resulting P-SIVR probability can be expanded as a series on the net number n of phonons emitted or absorbed during the collision, where the term for $n = 0$, P0-SIVR, corresponds to the elastic scattering without net phonon exchange, but including intermediated phonon transitions.

The P0-SIVR probability for the scattering $\mathbf{K}_i \rightarrow \mathbf{K}_f$, with \mathbf{K}_i (\mathbf{K}_f) being the initial (final) projectile momentum, can be expressed as a function of an effective transition amplitude $\mathcal{A}^{(P0-SIVR)}$ as [10]

$$\frac{dP^{(P0-SIVR)}}{d\Omega_f} = K_f^2 \left| \mathcal{A}^{(P0-SIVR)} \right|^2, \quad (1)$$

where $K_f = K_i$ as a result of the energy conservation and $\Omega_f = (\theta_f, \varphi_f)$ determines the \mathbf{K}_f direction, with θ_f and φ_f being the final polar and azimuthal angles measured with respect to the surface plane and the axial channel, respectively. The effective P0-SIVR amplitude reads [10]

$$\begin{aligned} \mathcal{A}^{(P0-SIVR)} &= \int d\mathbf{R}_o f(\mathbf{R}_o) \int d\mathbf{K}_o g(\mathbf{K}_o) \\ &\times \int d\mathbf{u}_o a_0(\mathbf{R}_o, \mathbf{K}_o, \mathbf{u}_o), \end{aligned} \quad (2)$$

where the functions f and g describe the position and momentum profiles, respectively, of the incident projec-

tile wave-packet, and $a_0(\mathbf{R}_o, \mathbf{K}_o, \mathbf{u}_o)$ is the partial amplitude corresponding to the classical projectile trajectory $\mathbf{R}_t \equiv \mathbf{R}_t(\mathbf{R}_o, \mathbf{K}_o, \mathbf{u}_o)$, which starts at the initial time $t = 0$ in the position \mathbf{R}_o with momentum \mathbf{K}_o . The trajectory \mathbf{R}_t depends also on the spatial configuration \mathbf{u}_o of the crystal at $t = 0$, where the underlined vector \mathbf{u}_o denotes the $3N$ -dimension vector associated with the spatial displacements of the N ions contained in the crystal sample, with respect to their equilibrium positions. Such crystal deviations are considered invariable during the collision time, which is much shorter than the characteristic time of phonon vibrations [27]. In addition, the partial amplitude $a_0(\mathbf{R}_o, \mathbf{K}_o, \mathbf{u}_o)$ includes an explicit dependence on \mathbf{u}_o through the momentum-dependent Debye-Waller factor, which acts as an effective screening of the atom-surface interaction. The complete expression of this partial amplitude, along with the steps used to derive the P0-SIVR approach, can be found in Ref. [10].

III. RESULTS

Our study is confined to 5 keV ^4He atoms grazingly impinging on a LiF(001) surface along the $\langle 110 \rangle$ channel, with different normal energies in the 0.1-3 eV range. For these collision system and incidence conditions experimental angular distributions were recently reported in Fig. 16 of Ref. [12].

To determine the influence of phonon effects, in all the cases the final projectile distributions obtained from the P0-SIVR approach, which includes intermediate phonon transitions, are compared with those derived from the SIVR approximation, which assumes an ideal rigid crystal surface. Both calculations - P0-SIVR and SIVR - were carried out using the same binary interatomic potentials, taken from Ref. [28], to build the pairwise additive surface potential. Furthermore, since the general features of the GIFAD patterns depend on the collimating conditions of the incident beam [29], we chosen a fixed collimation scheme, formed by a square slit of size $d = 0.09$ mm placed at a distance $L = 36$ cm from the surface, with an angular beam dispersion of 0.006 deg. These collimating parameters, which are in accord with current experimental setups for GIFAD [12, 23], were used to evaluate the spatial and momentum profiles of the incident wave-packet as given in Ref. [21]. Details of the P0-SIVR and SIVR calculations can be respectively found in Refs. [10, 11] and [21, 30].

A. Dependence of the phonon effects on E_\perp

We start by considering a low normal energy for He/LiF GIFAD [16], $E_\perp = 0.175$ eV, for which helium projectiles probe regions far from the topmost crystal layer, with He-surface distances $Z \geq 1.9$ Å, suggesting a minor role of lattice vibrations. In Figs. 1 (a) and 1 (b) we respectively show the SIVR and P0-SIVR two-

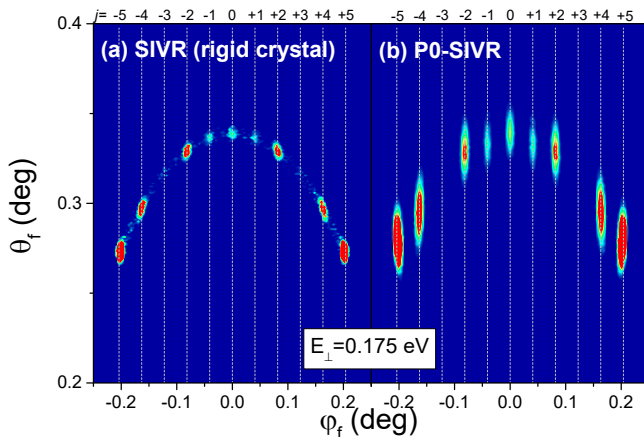


FIG. 1: (Color online) Two-dimensional projectile distributions, as a function of θ_f and φ_f , for 5 keV ${}^4\text{He}$ atoms scattered off LiF(001) at the temperature $T = 300$ K. Incidence along the (110) channel with the normal energy $E_\perp = 0.175$ eV is considered. Results derived within (a) the SIVR approximation, for a rigid crystal, and (b) the P0-SIVR approach, including thermal vibrations, are displayed. Vertical dashed lines indicate the ideal positions of the Bragg peaks, with orders $j = 0, \pm 1, \dots$

dimensional distributions for $E_\perp = 0.175$ eV, as a function of the final polar and azimuthal angles. Except for the different polar spreads, both angular distributions are very alike: They present similar interference structures, with less intense Bragg peaks of order $j = 0, \pm 1$, and missing $j = \pm 3$ peaks. Moreover, the azimuthal positions of the Bragg maxima ($\varphi_j^{(B)}$, with $j = 0, \pm 1, \pm 2, \dots$) are not affected by the thermal fluctuations of the crystal atoms, being $\varphi_j^{(B)} = \arcsin(j\lambda/a_y)$, with $\lambda = 2\pi/K_i$ and $a_y = 5.4$ a.u. the channel width. This latter behavior was found to be independent of the E_\perp value, being related to the average of the spatial deviations of a large number of crystal atoms involved in the scattering process. However, despite the low normal energy considered in Fig. 1, the lattice vibrations produce a wide polar dispersion of the Bragg maxima, transforming the small spots on the Laue circle, displayed in Fig. 1 (a), into vertical streaks, as it is observed in Fig. 1 (b).

In Fig. 2 we compare SIVR and P0-SIVR distributions for higher normal energies: $E_\perp = 0.635, 0.870$, and 1.320 eV. When E_\perp increases, more equally φ_f -spaced Bragg peaks are visible in the angular distributions. But again, the most noticeable effect introduced by lattice vibrations is the polar dispersion of the GIFAD patterns. The P0-SIVR distributions for the different E_\perp values (right-column of Fig. 2) display a broad polar spread that gives rise to a thick annulus, with mean radius θ_i , which contrast with the thin Laue circle observed for the SIVR distributions derived by assuming a rigid crystal (left-column). Furthermore, the P0-SIVR interference structures start to blur as E_\perp becomes higher than 1

eV, as a consequence of the decoherent effect produced by phonon contributions. For $E_\perp = 1.320$ eV, the P0-SIVR distribution of Fig. 2 (f) shows a more diffuse GIFAD pattern than those for the lower E_\perp values, shown in the upper panels of Fig. 2. Instead, the SIVR distributions exhibit well defined sharp maxima in all the panels of Fig. 2, without smudging for high normal energies.

B. Decoherent phonon effects

In order to analyze in more detail the decoherent effect of lattice vibrations on GIFAD patterns, in Fig. 3 we plot the projected intensities, as a function of the deflection angle $\Theta = \arctan(\varphi_f/\theta_f)$, for the cases of Fig. 2. For $E_\perp = 0.635, 0.870$, and 1.320 eV, the differential P0-SIVR probabilities $dP^{(P0-SIVR)}/d\Theta$, derived from Eq. (1) by integrating over a reduced annular area of central thickness 0.005 deg [31], are displayed along with the corresponding SIVR values normalized at $\Theta = 0$. For the three normal energies, thermal fluctuations affect the relative intensities of the interference maxima, mostly decreasing the intensity of some Bragg peaks. This thermal effect on $dP^{(P0-SIVR)}/d\Theta$ is partially related to the polar dispersion of the P0-SIVR maxima because some of them are shifted above or below the ideal Laue circle, as also observed in the experiment [12], affecting the result of the integral over θ_f involved in the projection method [31]. Moreover, for $E_\perp = 1.320$ eV phonon-mediated processes included in the P0-SIVR approach give rise to a decoherent effect in the Θ - spectrum, which smudges several interference maxima, as it is seen in Fig. 3 (c).

Finally, in Fig. 4 we contrast the angular distributions derived within the SIVR and P0-SIVR approximations for $E_\perp = 3$ eV. At this high normal energy, for which helium atoms reach closest approach distances to the surface of about $Z \simeq 0.85$ Å, the SIVR distribution for a rigid crystal still exhibits well-defined Bragg maxima over a thin ring (Fig. 4 (a)). But remarkably, these interference structures completely disappear when phonon contributions are taken into account through the P0-SIVR approach, as it is showed in Fig. 4 (b). Notice that at $E_\perp = 3$ eV, a similar decoherent effect was experimentally reported in Fig. 16 of Ref. [12]. Therefore, these findings suggest that the decoherence introduced by thermal vibrations when helium projectiles move close to the surface plane is able to destroy the quantum interference, making the projectile distributions tend to the classical limit.

In relation to the comparison with the available experimental data, the P0-SIVR distributions displayed in Figs. 1, 2, and 4 reproduce fairly well the overall features of the experimental ones shown in Fig. 16 of Ref. [12]. However, we found visible differences in the relative intensities of the diffraction maxima for several normal energies. Taking into account that GIFAD patterns are extraordinarily sensitive to the atom-surface potential, these discrepancies could be attributed to deficiencies of

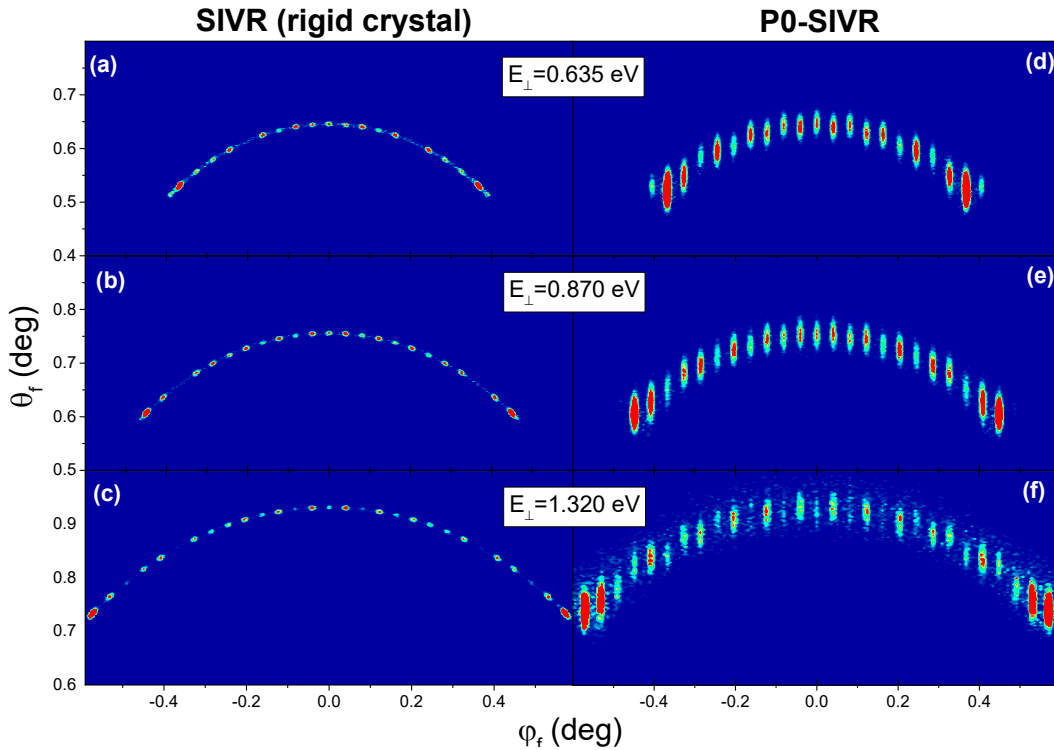


FIG. 2: (Color online) Analogous to Fig. 1 for the following normal energies: (a) and (d), $E_{\perp} = 0.635$ eV; (b) and (e), $E_{\perp} = 0.870$ eV; and (c) and (f), $E_{\perp} = 1.320$ eV. Panels (a), (b), and (c) (left column) show angular distributions for a rigid crystal derived within the SIVR approximation, while panels (d), (e), and (f) (right column) display P0-SIVR angular distributions including effects due to thermal lattice vibrations.

the pairwise additive potential model [28]. In particular, at the normal energy $E_{\perp} = 3$ eV, the absence of any signature of a central peak in the P0-SIVR distribution of Fig. 4 (b), in opposition to the experiment, would suggest that our potential model [28] is not able to properly describe the He-LiF(001) interaction at short distances. Furthermore, despite the large number of trajectories (more than 10^7) used in the P0-SIVR calculations displayed in Fig. 4 (b), the rainbow maxima are more diffuse than those observed in the experimental angular distribution [12], which shows outermost oval spots.

C. Phonon effects on the polar profile

Since the polar dispersion is the main phonon effect on GIFAD patterns, in this subsection we thoroughly analyze the dependence on the normal energy of the polar profiles corresponding to different Bragg maxima. In Fig. 5 we plot the polar distribution of the central maximum, obtained from the P0-SIVR approach, for $E_{\perp} = 0.365$, 0.635, and 0.870 eV. In each panel, the differential probability $dP^{(P0-SIVR)}/d\theta_f$ at $\varphi_f = 0$ is compared with the SIVR polar profile derived from a rigid crystal model, which displays a sharp peak at the specular reflection angle $\theta_f = \theta_i$. In contrast, the polar distributions derived

within the P0-SIVR approach present a broad asymmetric maximum, peaked at the Laue circle, which is due to the contribution of phonon-mediated processes. We found that the θ_f -asymmetry with respect to the Laue circle depends on the normal energy, with a more extended polar distribution below the Laue circle for $E_{\perp} = 0.870$ eV, and the inverse behavior for $E_{\perp} = 0.365$ and 0.635 eV.

In addition, in Fig. 5 we also show that the P0-SIVR polar profiles can be well reproduced by the lognormal function

$$\mathcal{P}(\theta_f) = \frac{A}{\omega \theta_f} \exp\left[-\frac{2(\ln(\theta_f/\theta_c))^2}{\omega^2}\right], \quad (3)$$

as it is usually done to deal with the experimental data [8, 12, 13], where A , θ_c , and ω are fitting parameters. From this fitting procedure we can determine the log-normal width ω of the P0-SIVR central peak, which is plotted as a function of E_{\perp} in Fig. 6 (square symbols). Noticeably, the ω values derived from the P0-SIVR approach do not suffer significant changes as the normal energy varies, running along a horizontal dot-dashed line in Fig. 6. A similar polar behavior was reported in a recent experimental study for a lower normal energy range [13].

As observed in Fig. 6, the experimentally-derived log-normal widths extracted from Fig. 7 of Ref. [13], which

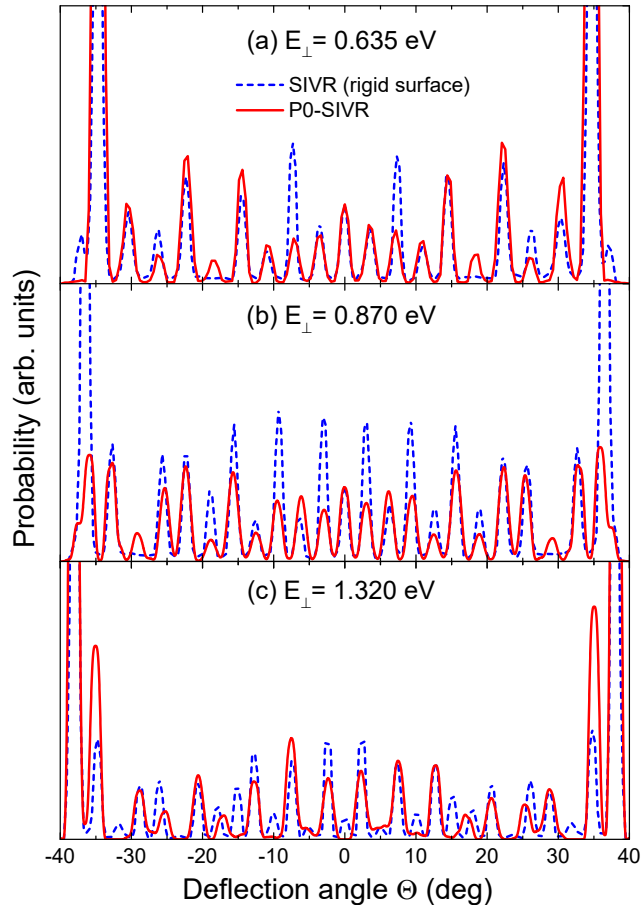


FIG. 3: (Color online) Differential probabilities as a function of the deflection angle $\Theta = \arctan(\varphi_f/\theta_f)$, for different normal energies: (a) $E_{\perp} = 0.635$ eV, (b) $E_{\perp} = 0.870$ eV, and (c) $E_{\perp} = 1.320$ eV. In all the panels, red solid line, P0-SIVR probability including thermal vibrations; blue dashed line, SIVR probability for a rigid crystal.

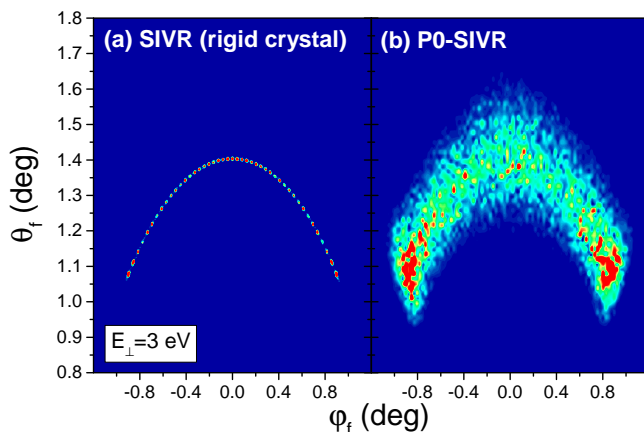


FIG. 4: (Color online) Analogous to Fig. 1 for the normal energy $E_{\perp} = 3$ eV.

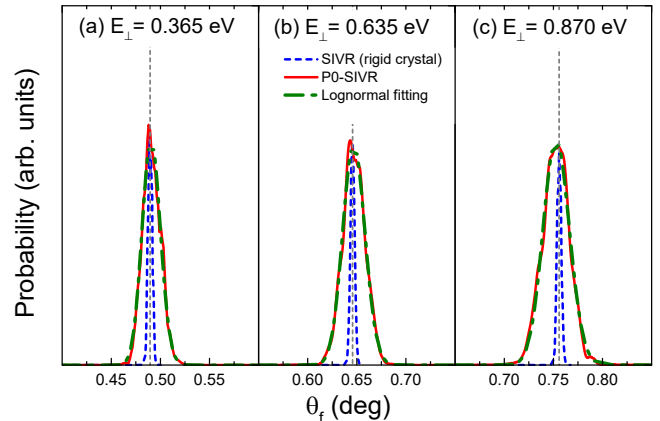


FIG. 5: (Color online) Intensity profile of the central maximum at $\varphi_f = 0$, as a function of the polar angle θ_f , for different normal energies: (a) $E_{\perp} = 0.365$ eV, (b) $E_{\perp} = 0.635$ eV, and (c) $E_{\perp} = 0.870$ eV. In all the panels, red solid line, differential probability derived within the P0-SIVR approach; blue dashed line, SIVR probability for a rigid crystal; green dot-dashed line, lognormal fitting of the P0-SIVR results, as given by Eq.(3). Vertical gray dashed line, ideal θ_f -position on the Laue circle (i.e., $\theta_f = \theta_i$).

are also shown in the inset [32], tend to an asymptotic constant limit as E_{\perp} increases. Then, to compare with these experimental data, obtained under different incidence conditions, we extrapolate the experimental limit to higher normal energies, finding that the lognormal width of the central peak of the P0-SIVR distribution underestimates this extrapolated limit by a factor 3. This fact would indicate the importance of phonon-mediated scattering with net phonon exchange, which might contribute to the polar dispersion of the interference patterns, as considered in recent articles [8, 13]. However, notice that the experimentally-derived data of Ref. [13] take into account the addition of polar profiles corresponding to different Bragg orders. If the polar width of the outermost P0-SIVR peaks is evaluated as a function of E_{\perp} , the results, plotted with triangle symbols in Fig. 6, run a factor 2 below the experimental asymptotic limit, reducing the simulation-experiment gap.

IV. CONCLUSIONS

In this work, we have study the dependence on the normal energy of the lattice vibration effects that affect the GIFAD patterns for He/LiF(001) at room temperature. Our analysis was based on the P0-SIVR approximation [10], which is a semiquantum method that describes the zero-phonon scattering process, including the contribution of intermediate phonon transitions. In accord with previous experimental and theoretical studies [8, 11–14], we found that the main effect introduced by

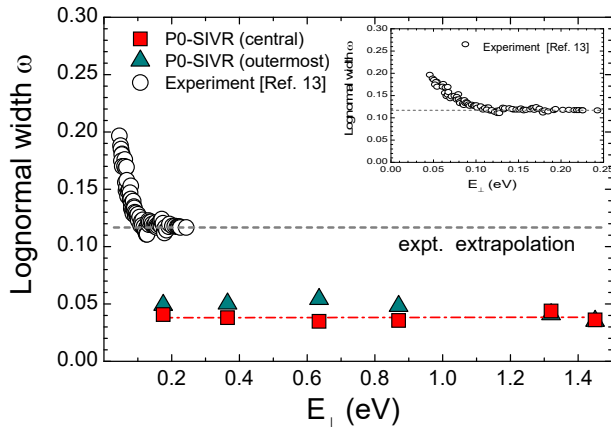


FIG. 6: (Color online) Lognormal width ω of the distribution given by Eq. (3), as a function of the normal energy. Theory: Solid squares and triangles, values derived by fitting P0-SIVR results for the central and outermost peaks, respectively. The red dot-dashed line corresponds to the linear fitting of the P0-SIVR lognormal width of the central peak. Experiment: Empty circles, experimentally-derived data extracted from Fig. 7 of Ref. [13]. The black dashed line indicates the experimental asymptotic limit. Inset: Details of the experimentally-derived data [13].

the phonon contributions is a wide polar dispersion of the interference structures, which is present even at low normal energies. For normal energies in the 0.1-1.5 eV range, the azimuthal positions of the Bragg peaks coincide with those derived from an ideal rigid crystal, but the relative intensities of some Bragg orders are modified by the lattice fluctuations as the normal energy increases, indicating that thermal effects should be taken into account

in order to use GIFAD as a surface analysis technique.

Furthermore, we observe that the interference patterns start to blur for $E_{\perp} \gtrsim 1.3$ eV, vanishing completely at $E_{\perp} \gtrsim 3$ eV due to the decoherent effect produced by the thermal vibrations of the LiF crystal. At high normal energies, analogous non-coherent experimental distributions were recently reported in Ref. [12]. We found that the P0-SIVR approach reproduces fairly well the overall features of the experimental data of Fig. 16 of Ref. [12]. However, it should be mentioned that in several cases, the relative Bragg intensities of the simulated patterns are not in full agreement with the experiment. Such discrepancies might be attributed to the atom-surface interaction, whose proper description represents a real challenge for the potential models.

Concerning the polar profiles of the P0-SIVR distributions, they are well fitted with a lognormal function, as it happens with the experiments [13]. Within the P0-SIVR approach, the polar lognormal width ω of the central maximum remains constant over the 0.1-1.5 eV normal energy range. This behavior is in agreement with recent experimentally-derived data for lower normal energies [13]. Nevertheless, present P0-SIVR ω -values underestimate the experimental asymptotic limit by a factor about 2, which would indicate that there are other mechanisms, like inelastic phonon-mediated processes involving net phonon exchange [12, 13], which might contribute to the polar spread.

Acknowledgments

The authors acknowledge financial support from CONICET and ANPCyT of Argentina.

-
- [1] A. Schüller, S. Wethekam, and H. Winter. *Phys. Rev. Lett.*, 98:016103, 2007.
 - [2] P. Rousseau, H. Khemliche, A. G. Borisov, and P. Roncin. *Phys. Rev. Lett.*, 98:016104, 2007.
 - [3] C. Díaz and M. S. Gravielle. *Phys. Chem. Chem. Phys.*, 24:15628–15656, 2022.
 - [4] P. Atkinson, M. Eddrief, V. H. Etgens, H. Khemliche, M. Debiossac, A. Momeni, M. Mulier, B. Lalmi, and P. Roncin. *Appl. Phys. Lett.*, 105:021602, 2014.
 - [5] F. Aigner, N. Simonović, B. Solleder, L. Wirtz, and J. Burgdörfer. *Phys. Rev. Lett.*, 101:253201, 2008.
 - [6] P. Rousseau, H. Khemliche, N. Bundaleski, P. Soullisse, A. Momeni, and P. Roncin. *J. Phys.: Conf. Ser.*, 133:012013, 2008.
 - [7] A. Schüller, S. Wethekam, D. Blauth, H. Winter, F. Aigner, N. Simonović, B. Solleder, J. Burgdörfer, and L. Wirtz. *Phys. Rev. A*, 82:062902, 2010.
 - [8] P. Roncin and M. Debiossac. *Phys. Rev. B*, 96:035415, 2017.
 - [9] M. C. Schram and E. J. Heller. *Phys. Rev. A*, 98:022137, 2018.
 - [10] L. Frisco and M. S. Gravielle. *Phys. Rev. A*, 100:062703, 2019.
 - [11] L. Frisco and M. S. Gravielle. *Phys. Rev. A*, 102:062821, 2020.
 - [12] M. Debiossac, P. Pan, and P. Roncin. *Phys. Chem. Chem. Phys.*, 23:7615–7636, 2021.
 - [13] P. Pan, M. Debiossac, and P. Roncin. *Phys. Rev. B*, 104:165415, 2021.
 - [14] P. Pan, M. Debiossac, and P. Roncin. *Phys. Chem. Chem. Phys.*, 24:12319–12328, 2022.
 - [15] J. R. Manson, H. Khemliche, and P. Roncin. *Phys. Rev. B*, 78:155408, 2008.
 - [16] A. Schüller, H. Winter, M. S. Gravielle, J. M. Pruneda, and J. E. Miraglia. *Phys. Rev. A*, 80:062903, 2009.
 - [17] A. S. Muzas, F. Gatti, F. Martín, and C. Díaz. *Nucl. Instr. Meth. B*, 382:49–53, 2016.
 - [18] H. Winter and A. Schüller. *Prog. Surf. Sci.*, 86:169–221, 2011.
 - [19] M. S. Gravielle and J. E. Miraglia. *Phys. Rev. A*,

- 90:052718, 2014.
- [20] G. A. Bocan, J. D. Fuhr, and M. S. Gravielle. *Phys. Rev. A*, 94:022711, 2016.
- [21] M. S. Gravielle and J. E. Miraglia. *Phys. Rev. A*, 92:062709, 2015.
- [22] L. Frisco, J. E. Miraglia, and M. S. Gravielle. *J. Phys.: Condens. Matter*, 30:405001, 2018.
- [23] G. A. Bocan, H. Breiss, S. Szilasi, A. Momeni, E. M. Staicu-Casagrande, M. S. Gravielle, E. A. Sánchez, and H. Khemliche. *Phys. Rev. Lett.*, 125:096101, 2020.
- [24] G. A. Bocan, H. Breiss, S. Szilasi, A. Momeni, E. M. Staicu-Casagrande, E. A. Sánchez, M. S. Gravielle, and H. Khemliche. *Phys. Rev. B*, 104:235401, 2021.
- [25] W. H. Miller. *J. Phys. Chem A*, 105:2942–2955, 2001, and references therein.
- [26] D. P. Dewangan and J. Eichler. *Phys. Rep.*, 247:59–219, 1994.
- [27] N. W. Ashcroft and N. D. Mermin. *Solid State Physics*. Brooks/Cole, Cengage Learning, Belmont, USA, 1976.
- [28] J. E. Miraglia and M. S. Gravielle. *Phys. Rev. A*, 95:022710, 2017.
- [29] J. Seifert, J. Lienemann, A. Schüller, and H. Winter. *Nucl. Instrum. Methods Phys. Res. B*, pages 99–105.
- [30] M. S. Gravielle, J. E. Miraglia, and L. Frisco. *Atoms*, 6:64, 2018.
- [31] M. Debiossac and P. Roncin. *Nucl. Instr. Methods Phys. Res. B*, 382:36–41, 2016.
- [32] The lognormal widths extracted from Fig. 7 of Ref. 13 were multiplied by 2 in accord with Eq. (3).